J. Plasma Physics (1999), *vol.* 61, *part* 2, *pp.* 191–212. Printed in the United Kingdom

Charge-separation velocity shear and suppression of turbulence at a plasma edge in the gyrokinetic approximation

M. SHOUCRI,[1] G. MANFREDI,[2] P. BERTRAND,[2] A. GHIZZO,[2] J. LEBAS,[2] G. KNORR,[3] E. SONNENDRUCKER,[2] H. BÜRBAUMER,[4] W. ENTLER,[4] G. KAMELANDER[4] and E. POHN[4]

[1] Centre Canadien de Fusion Magnétique, Varennes, PQ, Canada J3X 1S1
[2] LPMI-URA835 CNRS, Université Henri Poincaré, Nancy, France
[3] Department of Physics and Astronomy, University of Iowa, Iowa City, IA 52242, USA
[4] Osterreichisher Forschungzentrum Seibersdorf, Austria

(Received 27 May 1998 and in revised form 26 August 1998)

The existence and time evolution of charge separation at a plasma edge is studied using a code in which both ions and electrons are described by gyrokinetic equations that include the finite-Larmor-radius correction and the polarization drift. The ion finite-Larmor-radius effect allows the existence of charge separation between ions and electrons, and the polarization drift, which has opposite signs for ions and electrons, has a tendency to accentuate the charge separation in a time-varying electric field. We compare our results with those previously obtained using a code in which the ions were described by using a fluid guiding-centre model, and only the electrons were treated kinetically. In particular, we present results showing excellent agreement between the two codes on the transition of the spectrum of the nonlinear solution from a turbulent spectrum to one dominated by the fundamental mode, where the energy is condensing in the lowest-k modes (inverse cascade).

1. Introduction

The formation and existence of charge separation and an electric field at a plasma edge is an important problem in plasma-edge physics. This problem has received considerable attention in tokamak physics in connection with what is known as the L–H transition at the edge of a tokamak, which consists of a sudden increase in the plasma rotation accompanied by the creation of a radial electron field, which, by $\mathbf{E}\times\mathbf{B}$ drift, gives rise to a poloidal rotation (Burrell et al. 1990; Weynants et al. 1992). This drift is charge- and mass-independent. Important physical phenomena can be included in the study of this drift motion if we add the effect of the finite Larmor radius. In this case important new physics appears when spatial scales are close to the ion gyroradius and temporal scales are close to an ion gyroperiod. The effect of the finite Larmor radius is to allow the existence of charge separation between electrons and ions in the $\mathbf{E}\times\mathbf{B}$ flow. A powerful analysis of the two-dimensional finite-Larmor-radius guiding-centre equations was presented by Knorr and Pécseli (1989). This system has three 'rugged' quadratic invariants. A canonical-ensemble probability dis-

tribution characterized by three temperature states has been derived (Knorr and Pécseli 1989), and it has been shown that this system can have possible negative-temperature states, leading to an inverse cascade for the energy, with the equilibrium spectral energy density condensing in the low-k modes. Under these conditions, charges of equal sign tend to concentrate and form large vortices. Once this stage has been reached, the energy remains in the lowest-k modes. For the higher modes, less energy is available, so that the level of turbulence is significantly reduced.

The extension of this model by including polarization drift and a small dissipation in the form of a diffusion term was presented by Shoucri et al. (1997, 1998). The polarization drift has different signs for ions and electrons, and accentuates charge separation in a time-varying electric field. A small diffusion term simulates anomalous transport at the edge of the plasma. It was shown using this model that a small diffusion term can have an important effect on the evolution of charge separation at the edge of a plasma, which can be unstable, leading to a higher electric field and greater $\mathbf{E}\times\mathbf{B}$ drift at the plasma edge.

Manfredi et al. (1998) introduced kinetic effects in the guiding-centre equations for the electrons, while fluid guiding-centre equations were used for the ions. A study was presented on the evolution of the spectrum associated with the linear and nonlinear solutions (Kelvin–Helmholtz instabilities), and it was shown that as the magnetic field direction approaches the direction of the normal to the plane of the plasma, the nonlinear solution evolves from a turbulent solution to a solution dominated by the fundamental (lowest) k mode. This corresponds to a transition from a solution dominated by a diffusion in velocity space to a solution dominated by particle diffusion in space. The present work extends the results of Manfredi et al. (1998) by using kinetic guiding-centre equations for both the ions and the electrons. We have been able in the present work to confirm the results presented by Manfredi et al. (1998) concerning the transition from a nonlinear solution dominated by a turbulent spectrum to a nonlinear solution dominated by the fundamental mode when the magnetic field direction approaches the direction of the normal to the plane of the plasma. The present results offer a powerful kinetic self-consistent treatment for conditions under which the nonlinear solution for charge separation at a plasma edge, dominated by $\mathbf{E}\times\mathbf{B}$ drift, is turbulent or is dominated by the lowest-k mode. The effect of a small spatial-diffusion term on these solutions will be studied. This powerful kinetic treatment is effected using an Eulerian Vlasov code, which is discussed in the Appendix (see also Ghizzo et al. 1993; Manfredi et al. 1996).

2. The pertinent equations

The geometry, the equations and the numerical methods are essentially those presented by Manfredi et al. (1998). We consider a two-dimensional slab geometry, x being the periodic (poloidal) direction and y the non-periodic (radial) one. The magnetic field $\mathbf{B}$ is situated in the (x,z) plane and makes an angle θ with the x axis (see Fig. 1). So the two-dimensional charge separation is located in the (x,y) plane, and z is the homogeneous toroidal direction. We assume that the motion perpendicular to the magnetic field is completely described by the $\mathbf{E}\times\mathbf{B}$ and polarization drifts. We include in the equations a

https://doi.org/10.1017/S0022377898007338 Published online by Cambridge University Press

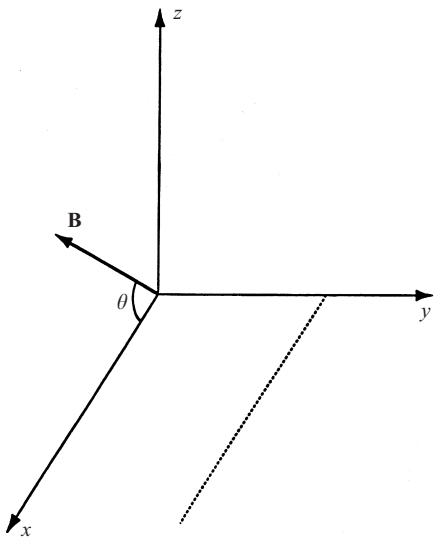

Figure 1. Geometry used for the numerical solution. The charge separation is in the (x, y) plane, and z is the homogeneous toroidal direction.

correction that takes into account the finite-Larmor-radius effect for the ions (the finite-Larmor-radius effect for the electrons is small, and is neglected), which allows the existence of charge separation between electrons and ions. Important physical phenomena can be added to the study of this drift motion if we include the effect of the finite ion Larmor radius. Furthermore, both species are assumed to be homogeneous in the z direction. With these assumptions, the gyrokinetic equations for electrons and ions are

$$\frac{\partial f_{i,e}}{\partial t}+\boldsymbol{\nabla}\cdot(\mathbf{v}_{\perp}f_{i,e})+v_{\parallel}\cos\theta\frac{\partial f_{i,e}}{\partial x}\pm\frac{e}{m_{i,e}}E_x^*\cos\theta\frac{\partial f_{i,e}}{\partial v_{\parallel}}=0, \tag{1a}$$

$$\mathbf{v}_{\perp}=\mathbf{v}_D+\mathbf{v}_{p_{i,e}}, \tag{1b}$$

$$\mathbf{v}_D=\frac{\mathbf{E}^*\times\mathbf{B}}{B^2}, \tag{1c}$$

$$\mathbf{v}_{p_{i,e}}=\pm\frac{m_{i,e}}{eB^2}\left[\frac{\partial\mathbf{E}_{\perp}^*}{\partial t}+(\mathbf{v}_D+\mathbf{v}_{\parallel})\cdot\boldsymbol{\nabla}_{\perp}\mathbf{E}_{\perp}^*\right]. \tag{1d}$$

Note that in our definition of the polarization drift we have neglected the term $\mathbf{v}_p\cdot\boldsymbol{\nabla}_{\perp}\mathbf{E}_{\perp}^*$, which would render (1d) an implicit definition of $\mathbf{v}_p$ (Shoucri et al. 1997). The subscripts i and e stand for ions (positive sign) or electrons (negative sign).

The asterisk indicates the action of an integral operator that takes into account the finiteness of the Larmor radius, and is defined by (Knorr and Pécseli 1989)

$$a^*(r)=\int G(r-r')a(r')\,dr', \tag{2}$$

where $G(r)$ is a Gaussian kernel. In Fourier space, this operation becomes a

https://doi.org/10.1017/S0022377898007338 Published online by Cambridge University Press

filtering operation, which is numerically easy to perform: each coefficient of the $e^{i\mathbf{k}\cdot\mathbf{r}}$ mode is multiplied by a factor $G_k = \exp(-\frac{1}{2}k_\perp^2\rho_{i,e}^2)$, where $\rho_{i,e}$ is the Larmor radius ($\rho_{i,e} = v_{ti,e}/\omega_{ci,e}$) for ions or electrons, and $k_\perp$ is the component of the wave vector perpendicular to the magnetic field (in our geometry, we have $k_\perp^2 = k_x^2\sin^2\theta + k_y^2$). Since the system is finite in the y direction, we convolute the function in (2) by first mirroring the function at the right boundary in y and thus doubling the y interval. We then take the Fourier transform and multiply the coefficients by $\exp(-\frac{1}{2}k_\perp^2\rho_i^2)$; the function is then Fourier-transformed back.

The Poisson equation is as follows:

$$\nabla^2\phi = -4\pi e(n_i^* - n_e^*), \tag{3}$$

$$\mathbf{E} = -\nabla\phi, \tag{4}$$

where $n_{i,e} = \int f_{i,e}\, dv_\parallel$, and the asterisk $n_{i,e}$ again indicates the filtering defined in (2). We note from (3) the charge created from the finite-gyroradius effect due to the difference $n_i^* - n_e^*$. Only when $n_i(y)$ has a gradient do we have $n_i^*(y) \equiv n_i(y)$, and this difference is greater the more important is the gradient. Hence it is the combined effect of the finite gyroradius, (2), and a gradient (as in a plasma edge) that gives an $n_i^*(y) \neq n_i(y)$, and hence results in the charge separation that appears in (3). The more important the gradient, the more important is the charge separation associated with it due to the finite ion gyroradius, and the more important is the self-consistent electric field calculated from (4).

Equations (1)–(4) constitute the mathematical model that we shall solve numerically. One of its peculiarities is that it couples the typical drift phenomena perpendicular to the magnetic field to the electron kinetic effects in the direction parallel to the magnetic field lines when the magnetic field is slightly tilted with respect to the normal (see Fig. 1). Details of the numerical scheme are presented in the Appendix.

3. Numerical results for $\theta = 89°$

We take, for both species, the following initial density profile (the same as in Manfredi et al. 1998):

$$N(y) = \tfrac{1}{2}(1 + \tanh 1.6y). \tag{5}$$

The initial conditions for ions and electrons are given by

$$f_{i,e}(x, y, v_\parallel, t = 0) = \frac{N(y)}{(2\pi T_{i,e})^{1/2}} e^{-v_\parallel^2/2T_{i,e}}(1 + \epsilon\sin k_0 x + \epsilon\sin 2k_0 x + \epsilon\sin 3k_0 x), \tag{6}$$

where a perturbation of amplitude equal to ϵ has been introduced. The relevant physical parameters, in dimensionless form, are chosen as follows:

$$\frac{T_e}{T_i} = 1, \qquad \frac{m_i}{m_e} = 1840, \qquad \frac{\omega_{ci}}{\omega_{pi}} = 0.9, \qquad \epsilon = 0.005.$$

Note that the actual parameter entering the equations with our normalization (see the Appendix) is the following:

$$\frac{\omega_{ce}}{\omega_{pe}} = \frac{\omega_{ci}}{\omega_{pi}}\left(\frac{m_i}{m_e}\right)^{1/2} = 0.9 \times \sqrt{1840}. \tag{7}$$

https://doi.org/10.1017/S0022377898007338 Published online by Cambridge University Press

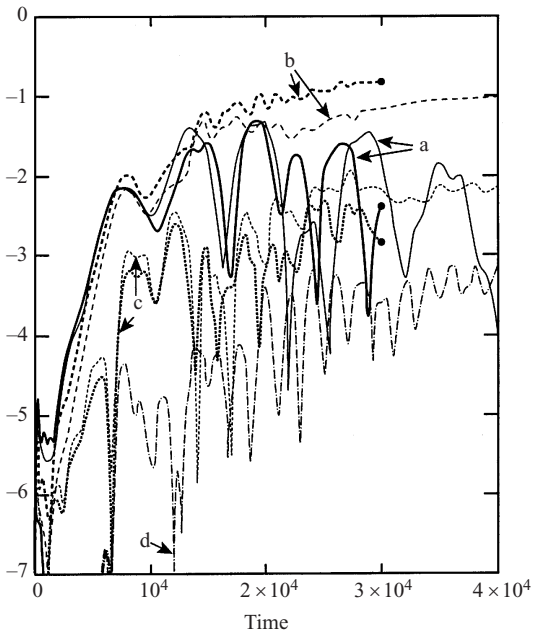

Figure 2. Time evolution of the logarithm of the first three Fourier modes calculated with the present code (kinetic equation for the ions, the curves a, b and c ending with a heavy dot at $\omega_{pe}t = 3\times10^4$), together with the time evolution of the first four Fourier modes calculated by Manfredi et al. (1998) up to $\omega_{pe}t = 4\times10^4$ (fluid guiding-centre equations for the ions).

The ion Larmor radius is therefore

$$\frac{\rho_i}{\lambda_{De}} = \frac{v_{Ti}/\omega_{ci}}{\lambda_{De}} = \frac{(T_i/T_e)^{1/2}}{\omega_{ci}/\omega_{pi}} = \frac{1}{0.9}. \tag{8}$$

The computational domain is the following:

$$0 \leqslant x \leqslant 28, \quad -6 \leqslant y \leqslant 6, \quad -5 \leqslant v_\parallel \leqslant 5,$$

the number of points is $N_x \times N_y \times N_v \equiv 64\times128\times128$, and the time step $\omega_{pe}\Delta t = 1$.

Our simulations were performed with a non-uniform temperature profile

$$T_{i,e}(y) = T_{i,e0}(0.2 + 0.4\tanh 1.6y), \tag{9}$$

with $T_{e0} = T_{i0} = 1$.

From the calculations presented by Manfredi et al. (1998), we repeat the calculations for $\theta = 89°$ and $89.5°$, since the transition from a nonlinear solution dominated by a turbulent spectrum to a nonlinear solution dominated by the fundamental k mode appeared between these two angles. The calculation for the first simulation with $\theta = 89°$ was carried up to $\omega_{pe}t = 3.0\times10^4$. The time evolutions of the first three harmonics are shown in Fig. 2 (curves a, b and c ending with a heavy dot), together with the first four harmonics previously presented for the same parameters by Manfredi et al. (1998) where the ions were treated with fluid guiding centre equations. The time evolutions of the first three modes are almost identical up to $\omega_{pe}t \approx 2\times10^4$. There is a small difference that develops afterwards, due to the fact that the motion and diffusion of the

https://doi.org/10.1017/S0022377898007338 Published online by Cambridge University Press

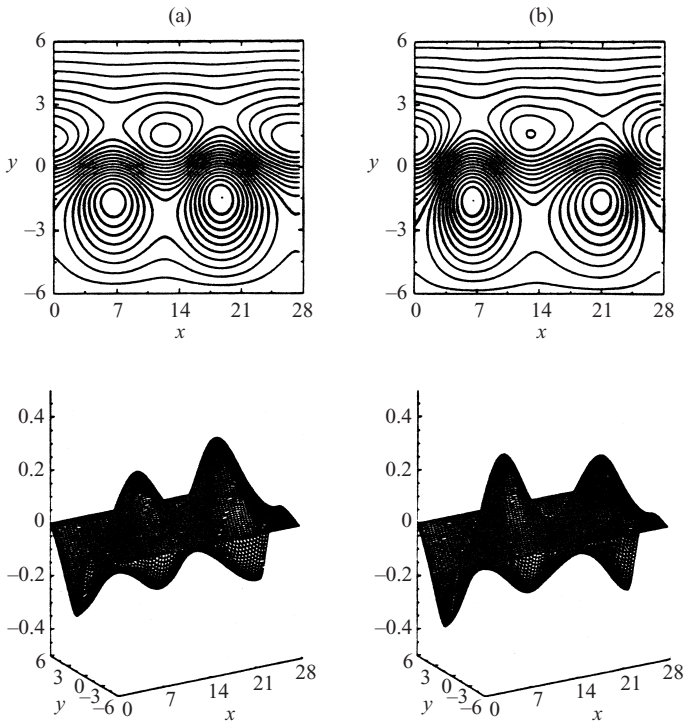

Figure 3. Contour plots and three-dimensional plots for the potential for $\theta = 89°$ at (a) $\omega_{pe}t = 1.8 \times 10^4$; (b) $\omega_{pe}t = 3.0 \times 10^4$.

ions in phase space calculated from the kinetic code are different from those calculated from the code with fluid ions, which only diffuses the ions in space. The nonlinear spectrum, however, is still turbulent and dominated by the second harmonic (although the curve b calculated with the present code is slightly higher for $\omega_{pe}t > 2 \times 10^4$ than the curve b calculated from the code with fluid equations for the ions in Manfredi et al. 1998). This dominance of the mode $2k_0$ is also clear in Fig. 3, which shows contour plots and three-dimensional plots of the potential. A two-dimensional contour plot of the distribution function (averaged over the y direction) at $\omega_{pe}t = 1.8 \times 10^4$ and 3.0×10^4 is presented in Fig. 4, together with a three-dimensional view of the plot, and shows the signature of the mode $2k_0$ essentially around small values of $v_\parallel$. The present code also provides us with the distribution function of the ions. Figure 5 shows at $\omega_{pe}t = 1.8 \times 10^4$ and 3.0×10^4 $(x, v_\parallel)$ plot of the ion distribution function integrated over y, as contour plots and three-dimensional plots.

The density profile as a function of y (the distribution function integrated over x and $v_\parallel$) is shown in Fig. 6 for the electrons (full curves) and for the smoothed ion density n_i^* (dotted curves). Figure 7 shows the profiles of the potential (full curves) and charge (dotted curves) averaged over x. Note the small deformation of the potential profile and the charge, since the dominant $2k_0$ mode and higher harmonics saturate at low level.

Test particles were used in order to sample some regions of phase space. These particles are put in selected regions of phase space and driven by the electric fields computed from the Vlasov simulation, although they do not themselves

https://doi.org/10.1017/S0022377898007338 Published online by Cambridge University Press

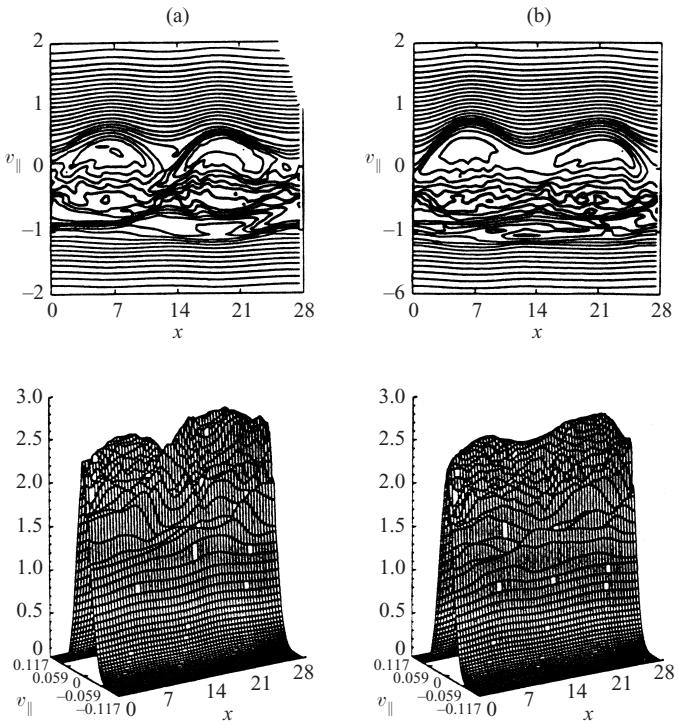

Figure 4. Contour plots of the electron distribution function (averaged over the y direction) in the $(x, v_\parallel)$ plane, together with three-dimensional views, at (a) $\omega_{pe}t = 1.8\times10^4$; (b) $\omega_{pe}t = 3.0\times10^4$.

contribute to the creation of the fields. The particles follow the characteristics of the Vlasov equation (1a), which, in our normalized units, are written as

$$\frac{dx}{dt} = E_y^* \frac{\sin\theta}{B} + v_{px} + v_\parallel \cos\theta, \tag{10a}$$

$$\frac{dy}{dt} = -E_x^* \frac{\sin\theta}{B} + v_{py}, \tag{10b}$$

$$\frac{dv_\parallel}{dt} = \pm \frac{e}{m_{i,e}} E_x^* \cos\theta, \tag{10c}$$

$$\frac{dw}{dt} = -w\boldsymbol{\nabla}\cdot\mathbf{v}_p. \tag{10d}$$

Equation (10d) comes from the fact that (1a) contains a source term of the form $f\boldsymbol{\nabla}\cdot\mathbf{v}_p$, since the polarization drift is not divergence-free. The quantity $w(t)$ is just a weight attached to each particle, reflecting the effect of this source term.

The evolution of the electrons in $(v_\parallel, y)$ space is shown in Fig. 8. This figure is particularly instructive. From (10), we see that an invariant of the motion would exist if $v_{py} = 0$. The expression of this invariant is easily found by dividing (10b) and (10c). When $v_{py} = 0$, we get

$$v_\parallel \pm \frac{eB}{m_{e,i}\tan\theta} y = \text{const.} \tag{11}$$

https://doi.org/10.1017/S0022377898007338 Published online by Cambridge University Press

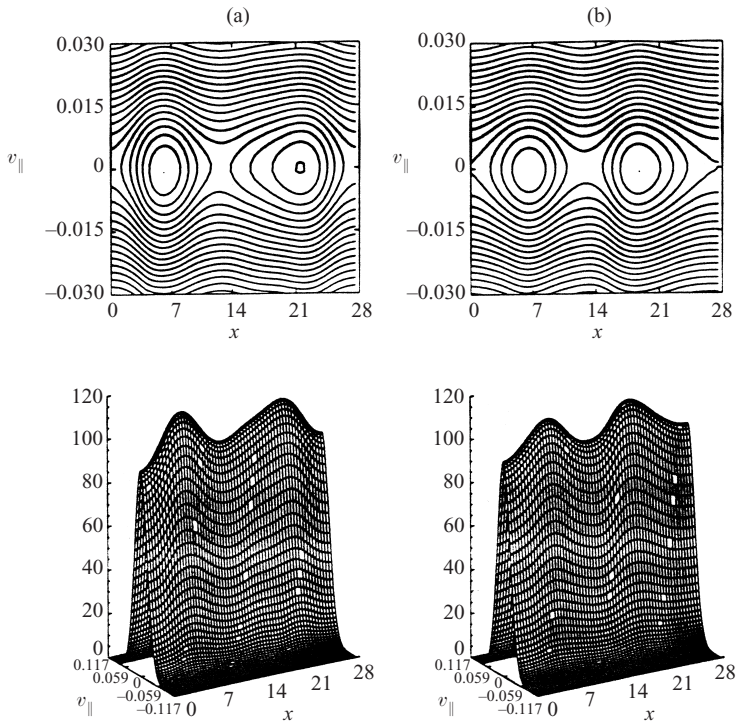

Figure 5. Contour plots of the ion distribution function (averaged over the y direction) in the $(x, v_\parallel)$ plane, together with a three-dimensional view, at (a) $\omega_{pe}t = 1.8 \times 10^4$; (b) $\omega_{pe}t = 3.0 \times 10^4$.

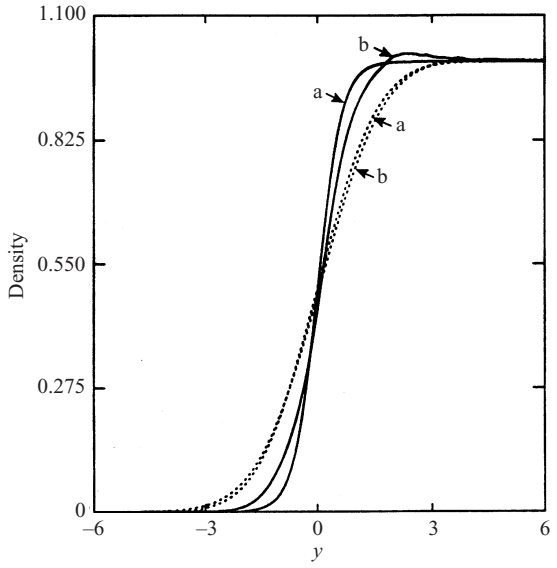

Figure 6. Density profiles as a function of y for the electrons (full curves) and the smoothed ions (dotted curves) at (a) $\omega_{pe}t = 0$; (b) $\omega_{pe}t = 3.0 \times 10^4$.

https://doi.org/10.1017/S0022377898007338 Published online by Cambridge University Press

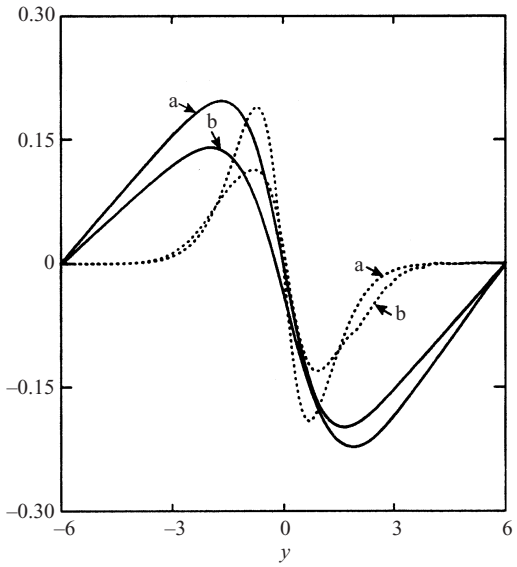

Figure 7. Profiles of the potential (full curves) and charge (dotted curves) spatially averaged over the periodic direction x at (a) $\omega_{pe}t = 0$; (b) $\omega_{pe}t = 3.0 \times 10^4$.

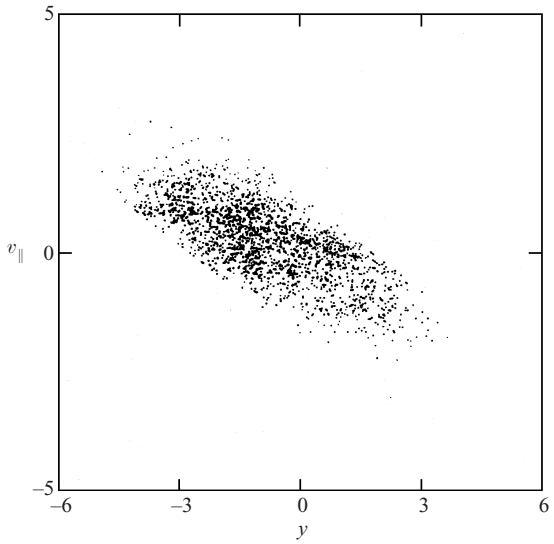

Figure 8. Electron test particles in $(v_\parallel, y)$ space at $\omega_{pe}t = 3.0 \times 10^4$. (The electrons were initially distributed uniformly at $-1 < v_\parallel < 1$ and $-2 < y < 1$.)

The invariant in (11) represents a straight line in $(y, v_\parallel)$ space. In Fig. 8 we show $(v_\parallel, y)$ space for the electrons at $\omega_{pe}t = 3.0 \times 10^4$. These electrons were initially uniformly loaded at $-1 < v_\parallel < 1$ (where the electron distribution function is distorted in Fig. 4) and $-2 < y < 1$ (along the gradient in y). They essentially show motion in a straight line according to (11), whose slope is given by $eB/(m_e \tan\theta)$. This is an indication that the effect of v_{py} is small for the electrons – as one would expect.

https://doi.org/10.1017/S0022377898007338 Published online by Cambridge University Press

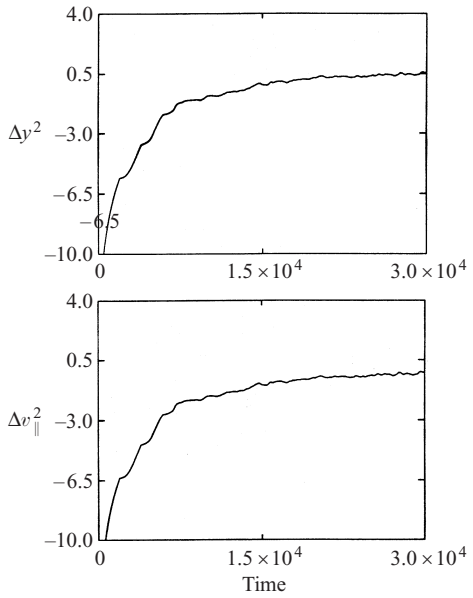

Figure 9. Plots of Δy^2 and $\Delta v_\parallel^2$ as functions of time for the electrons, calculated from (12) and (13).

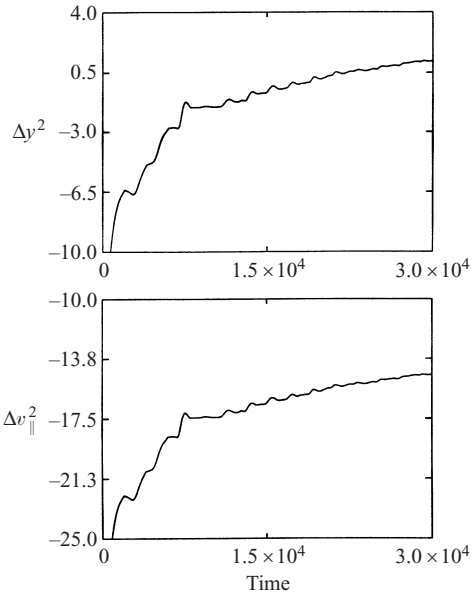

Figure 10. Plots of Δy^2 and $\Delta v_\parallel^2$ as functions of time for the ions, calculated from (12) and (13).

https://doi.org/10.1017/S0022377898007338 Published online by Cambridge University Press

We have subsequently calculated the mean-square displacements Δy^2 and $\Delta v_\parallel^2$, defined as (similar equations hold for electrons and ions)

$$\Delta y^2 = \frac{1}{N_{\rm part}} \sum_{i=1}^{N_{\rm part}} w_i(t)[y_i(t) - y_i(0)]^2, \tag{12}$$

$$\Delta v_\parallel^2 = \frac{1}{N_{\rm part}} \sum_{i=1}^{N_{\rm part}} w_i(t)[v_\parallel(t) - v_\parallel(0)]^2. \tag{13}$$

These quantities are related to the diffusion coefficients in space, D_y, and in velocity space, $D_{v_\parallel}$, by the following formulae:

$$D_y(t) = \frac{\Delta y^2}{t}, \qquad D_{v_\parallel} = \frac{\Delta v_\parallel^2}{t}. \tag{14}$$

The time evolutions of Δy^2 and $\Delta v_\parallel^2$ are shown in Fig. 9 for the electrons and in Fig. 10 for the ions. When the polarization drift is negligible, the weight $w(t)$ remains very close to its initial value $w(0) = 1$. In this case (11)–(14) gives the following result (written in our normalized units):

$$D_y = \frac{D_{v_\parallel} \tan^2 \theta}{\omega_{ce,i}^2}, \tag{15}$$

where $\omega_{ce,i}$ is the cyclotron frequency for electrons (ions) normalized to ω_{pe}. The diffusions in space y and in velocity space $v_\parallel$ are connected by (15). This constant ratio between D_y and $D_{v_\parallel}$ is clearly apparent in Figs 9 and 10, indicating again that for the parameters we have and for the results we are presenting, the polarization drift seems to play a minor role for the ions (it is neglected for the electrons).

4. Numerical results for $\theta = 89.5°$

Figure 11 shows the time evolutions of the first three Fourier modes calculated with the present code (curves ending with a heavy dot) up to $\omega_{pe}t = 1.2 \times 10^4$. We also present in the same figure the results obtained for the first four Fourier modes with the code using fluid equations for the ions in Manfredi et al. (1998) (calculated up to $\omega_{pe}t = 1.8 \times 10^4$). The agreement between the results obtained from the two codes is remarkable. The fundamental mode dominates slightly over the mode $2k_0$ towards the end. The two codes seem to agree on the angle θ at which there is a transition from a nonlinear solution dominated by a turbulent spectrum to a nonlinear solution dominated by the fundamental mode. Indeed, we do expect the fluid equations for the ions to become valid the closer θ is to 90°. Contour plots and three-dimensional plots for the potential are shown in Fig. 12, and agree very well with what has been presented by Manfredi et al. (1998). Note the vortices coalescing together in this case as the fundamental mode becomes dominant. Figure 13 shows the profiles of the potential and charge averaged over the periodic direction x. They show the potential profile evolving from a sine shape to a shape close to a half-sine when

https://doi.org/10.1017/S0022377898007338 Published online by Cambridge University Press

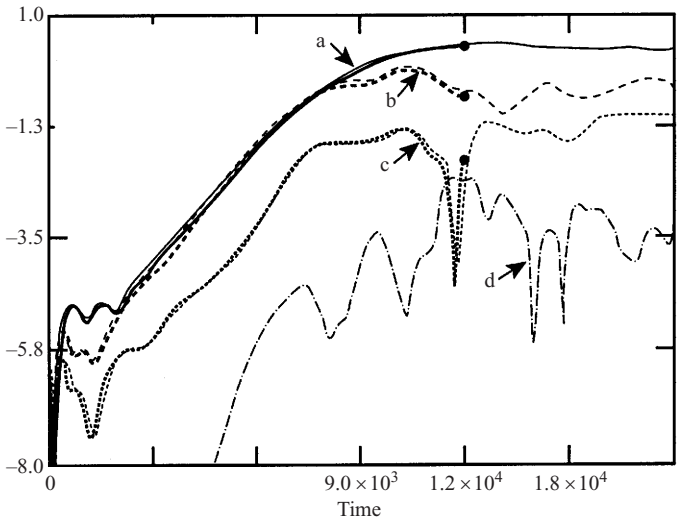

Figure 11. Time evolutions of the first three Fourier modes calculated with the present code (curves ending with a heavy dot up to $\omega_{pe}t = 1.2 \times 10^4$), and of the first four Fourier modes calculated with the code with fluid equations for the ions up to 1.8×10^4 (presented in Manfredi et al. 1998).

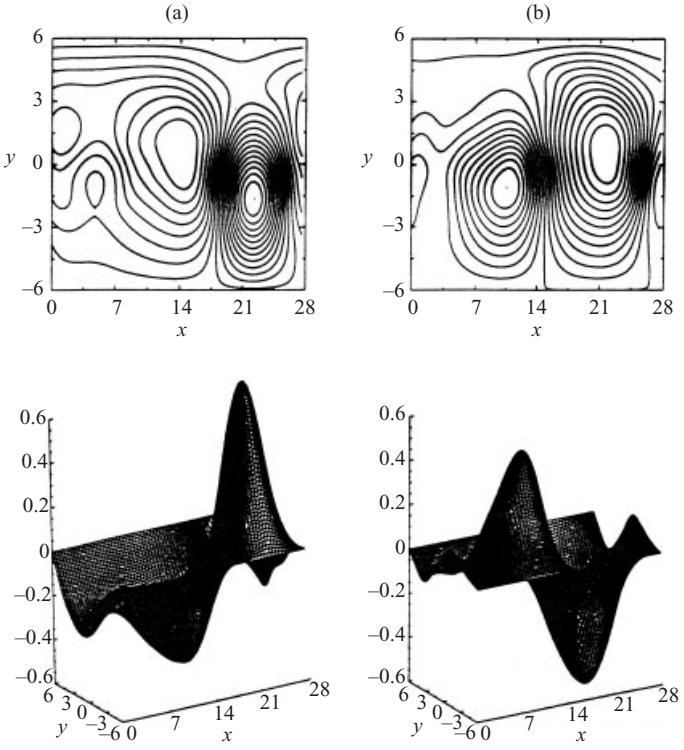

Figure 12. Contour plots and three-dimensional plots for the potential for $\theta = 89.5°$ at (a) $\omega_{pe}t = 1.0 \times 10^4$; (b) $\omega_{pe}t = 1.2 \times 10^4$.

https://doi.org/10.1017/S0022377898007338 Published online by Cambridge University Press

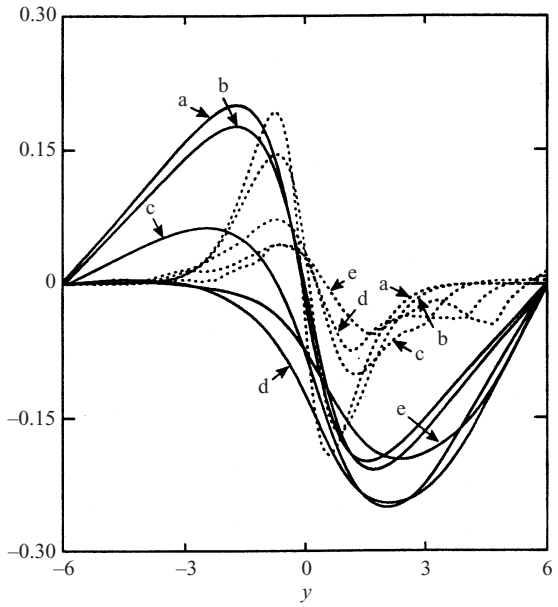

Figure 13. Profiles of the potential (full curves) and charge (dotted curves), averaged over the periodic direction x, for the case $\theta = 89.5°$, at (a) $\omega_{pe}t = 0$; (b) 6.0×10^3; (c) 8.0×10^3; (d) 1.0×10^4; (e) 1.2×10^4.

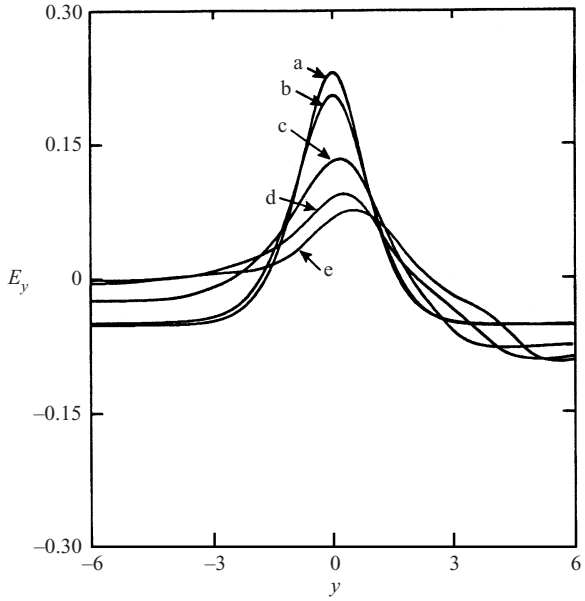

Figure 14. Profiles of the electric field E_y (spatially averaged over x) (note that $v_{Dx} \sim E_y$), for the case $\theta = 89.5°$, at (a) $\omega_{pe}t = 0$; (b) 6.0×10^3; (c) 8.0×10^3; (d) 1.0×10^4; (e) 1.2×10^4.

https://doi.org/10.1017/S0022377898007338 Published online by Cambridge University Press

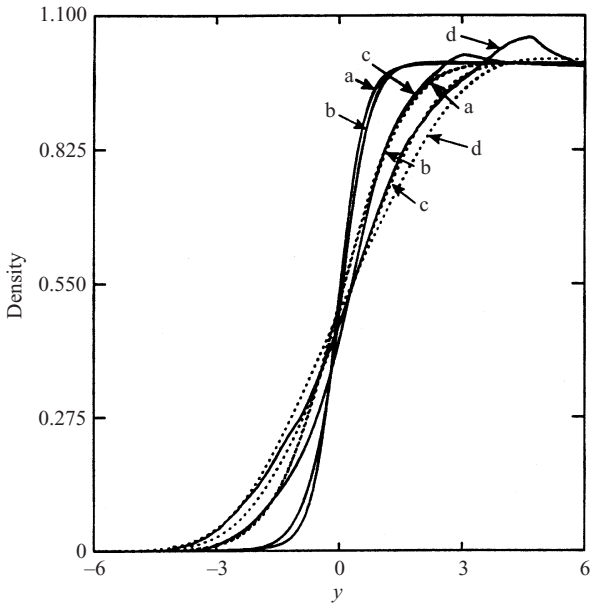

Figure 15. Profiles of the electron density (electron distribution function integrated over x and $v_{\|}$; full curves) and the smoothed ion density (dotted curves) at (a) $\omega_p t = 0$; (b) 6.0×10^3; (c) 8.0×10^3; (d) 1.2×10^4.

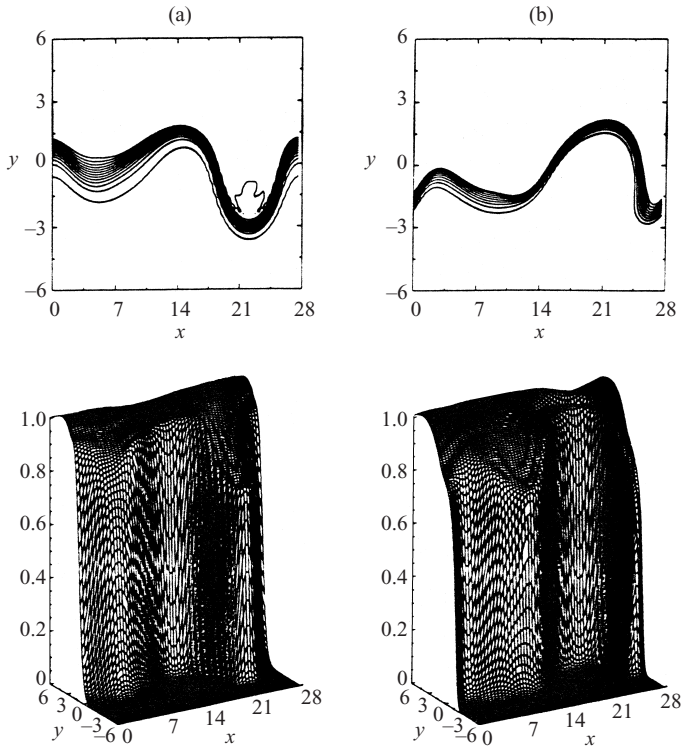

Figure 16. Contour plots and three-dimensional views for the ion density for the case with $\theta = 89.5°$, at (a) $\omega_{pe} t = 1.0 \times 10^4$; (b) $\omega_{pe} t = 1.2 \times 10^4$.

https://doi.org/10.1017/S0022377898007338 Published online by Cambridge University Press

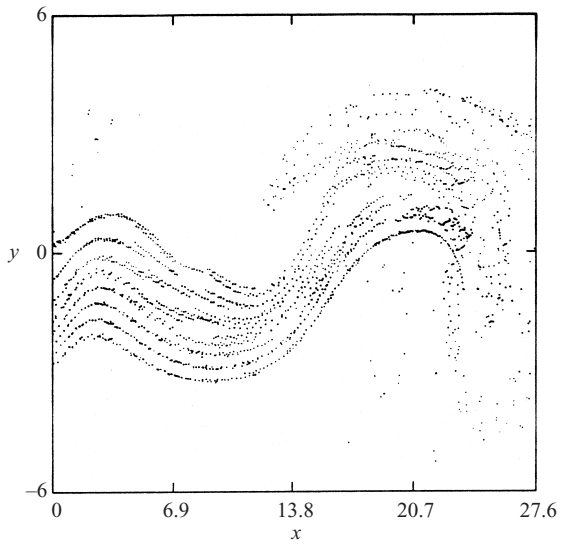

Figure 17. Ion test particles at $\omega_{pe}t = 1.2 \times 10^4$ (initially loaded uniformly in x, and between $-2 < y < 1$), and reproducing nicely the ion-density contours shown in Fig. 16 at $\omega_{pe}t = 1.2 \times 10^4$.

the fundamental mode becomes predominant, in agreement to what has been presented and discussed by Shoucri et al. (1997) and Manfredi et al. (1998), when θ is very close to 90°. The energy is cascading to the longest wavelength available in the system (condensing in the low-k modes) and the potential is distorting itself simultaneously to a shape close to a half-sine, at the same time where the fundamental mode is dominating in the periodic directory. The electric field E_y (spatially averaged over x) is shown in Fig. 14 (note that $v_{Dx} \sim E_y$).

The electron-density profiles (electron distribution function integrated over $v_\parallel$ and x) are shown in Fig. 15 (full curves), together with the smoothed ion-density profiles n_i^* (dotted curves) calculated from n_i using (2). Contour and three-dimensional plots for the ion density are shown in Fig. 16.

We followed, as in Sec. 3, the motion of test particles in phase space, in the self-consistent field calculated from the Vlasov code. Ions were initially loaded in (y, x) space uniformly in x, and between $-2 < y < 1$ in the y direction. At $\omega_{pe}t = 1.2 \times 10^4$, the distortion shown in Fig. 17 of the particles reproduces very well the ion-density contour shape presented in Fig. 16.

5. Effect of a spatial-diffusion term

We present in this section the effect of small spatial diffusion on the solution given in Sec. 4. Spatial-diffusion terms are important since anomalous transport is usually modelled by such a term. They can also be present in the numerical scheme (as in many particle codes), or added to smooth the microstructure that develops during a simulation and to control numerical instabilities. From the physical and numerical point of view, it is interesting to quantify the effect of a small diffusion term on the solution. We repeat the results for $\theta = 89.5°$ with

https://doi.org/10.1017/S0022377898007338 Published online by Cambridge University Press

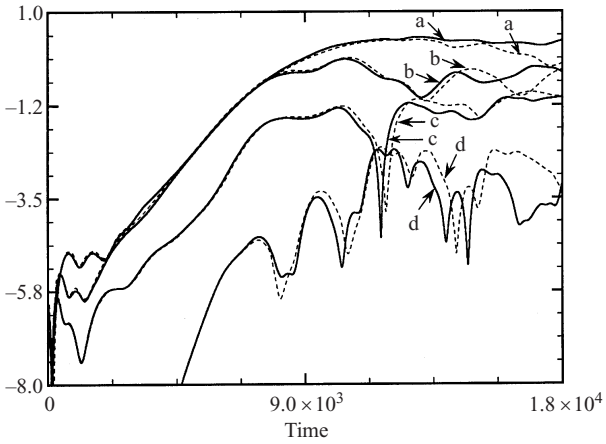

Figure 18. Time evolutions of the first three Fourier modes calculated for $\theta = 89.5°$ with $\nu_e = 0$ and $\nu_i = 0$ (similar to Fig. 11), and with $\nu_e = 5 \times 10^{-6}$ and $\nu_i = 2 \times 10^{-6}$ (dotted curves).

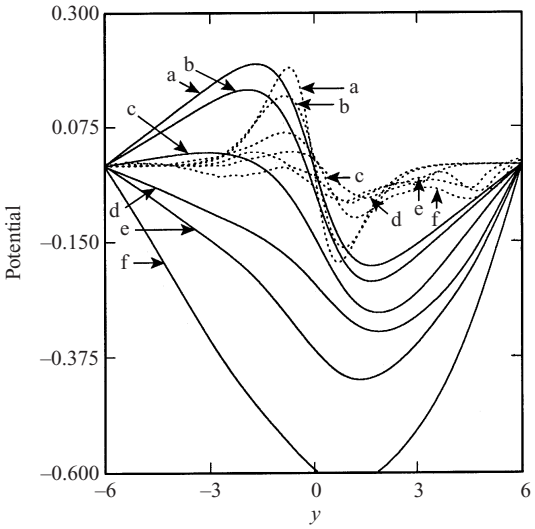

Figure 19. Profiles of the potential (full curves) and charge (dotted curves), averaged over the periodic direction x, for the case $\theta = 89.5°$, with $\nu_e = 5 \times 10^{-6}$ and $\nu_i = 2 \times 10^{-6}$, at (a) $\omega_{pe} t = 0$; (b) 6.0×10^3; (c) 8.0×10^3; (d) 1.2×10^4; (e) 1.4×10^4; (f) 1.8×10^4.

a spatial-diffusion term added to the equations as presented in the Appendix, with $\nu_e = 5 \times 10^{-6}$ and $\nu_i = 2 \times 10^{-6}$. Figure 18 shows the time evolution of the first three Fourier modes calculated for $\theta = 89.5°$ with $\nu_e = 0$ and $\nu_i = 0$ (full curves, similar to Fig. 11), and the first three Fourier modes for $\theta = 89.5°$ with $\nu_e = 5 \times 10^{-6}$ and $\nu_i = 2 \times 10^{-6}$ (dotted curves). The values of ν_e and ν_i are very small, and the difference between the full and dotted curves in Fig. 18 is minor. The effect on the charge distribution and the potential curves, however, is substantial. (Similar results were reported in Manfredi et al. (1996) for ITG

https://doi.org/10.1017/S0022377898007338 Published online by Cambridge University Press

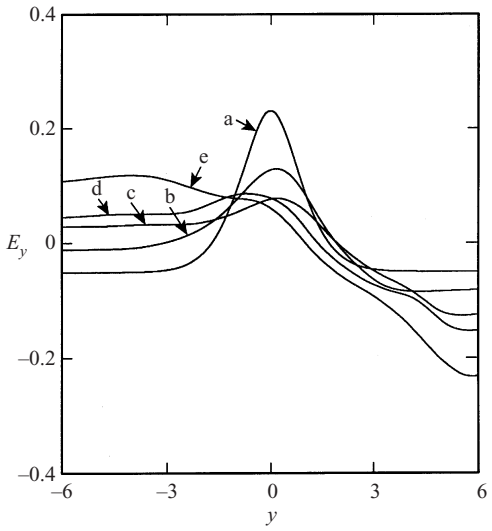

Figure 20. Profiles of the electric field E_y (spatially averaged over x) (note that $v_{Dx} \sim E_y$) for the case $\theta = 89.5°$, with $\nu_e = 5 \times 10^{-6}$ and $\nu_i = 2 \times 10^{-6}$, at (a) $\omega_{pe} t = 0$; (b) 8.0×10^3; (c) 1.2×10^4; (d) 1.4×10^4; (e) 1.8×10^4.

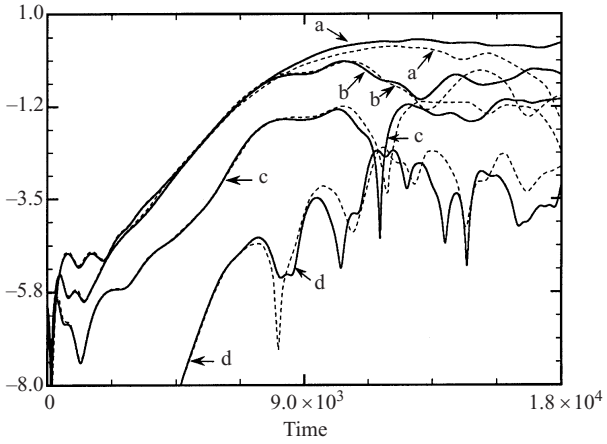

Figure 21. Time evolutions of the first three Fourier modes calculated for $\theta = 89.5°$ with $\nu_e = 0$ and $\nu_i = 0$ (similar to Fig. 11), and with $\nu_e = 1 \times 10^{-5}$ and $\nu_i = 2 \times 10^{-6}$ (dotted curves).

modes.) Figure 19 shows the profiles of the potential (full curves) and charge (dotted curves), averaged over the periodic direction x. Note the important increase in the potential, which is evolving to a complete half-sine, and the important increase in the value of E_y in Fig. 20, which is associated with the velocity v_{Dx}. Figures 21–23 present, for the case $\nu_e = 1 \times 10^{-5}$ (while ν_i is kept constant, $\nu_i = 2 \times 10^{-6}$), results similar to those presented in Figs 18–20. Although ν_e and ν_i are still very small, note the more important modifications in the time evolutions of the first three Fourier modes towards the end of the

https://doi.org/10.1017/S0022377898007338 Published online by Cambridge University Press

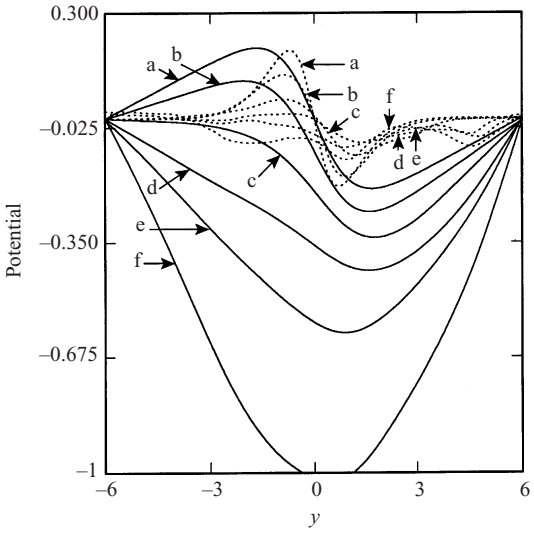

Figure 22. Profiles of the potential (full curves) and charge (dotted curves), averaged over the periodic direction x, for the case $\theta = 89.5°$, with $\nu_e = 1 \times 10^{-5}$ and $\nu_i = 2 \times 10^{-6}$, at (a) $\omega_{pe} t = 0$; (b) 6.0×10^3; (c) 8.0×10^3; (d) 1.2×10^4; (e) 1.4×10^4; (f) 1.8×10^4.

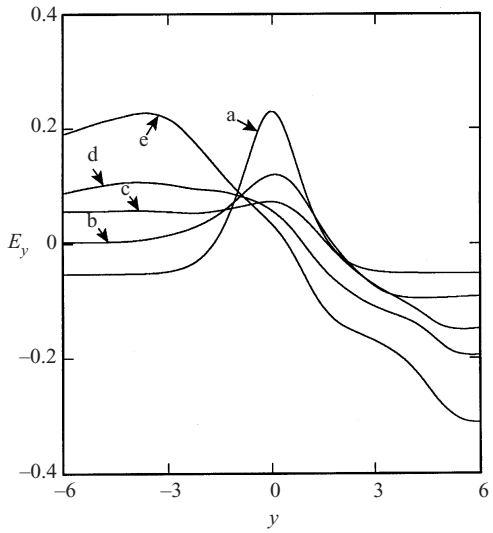

Figure 23. Profiles of the electric field E_y (spatially averaged over x) (note that $\nu_{Dx} \sim E_y$) for the case $\theta = 89.5°$, with $\nu_e = 1 \times 10^{-5}$ and $\nu_i = 2 \times 10^{-6}$, at (a) $\omega_{pe} t = 0$; (b) 8.0×10^3; (c) 1.2×10^4; (d) 1.4×10^4; (e) 1.8×10^4.

simulation (dotted curves in Fig. 20 compared with those in Fig. 18 and the more rapid evolution of the charge separation and substantial increase in the potential in Fig. 22. The increase in E_y (and ν_{Dx}) in Fig. 23 is again substantial. The result can even be an instability, as discussed by Shoucri et al. (1995).

https://doi.org/10.1017/S0022377898007338 Published online by Cambridge University Press

6. Conclusions

A code with gyrokinetic equations for both ions and electrons has been used to study the existence and time evolution of charge separation at a plasma edge. The equations include the finite-Larmor-radius correction for the ions and the polarization drift. We have compared our results with those previously obtained using a code in which the ions were described using a fluid guiding-centre model and only the electrons were treated kinetically. We have investigated in detail the two cases where $\theta = 89°$ and $\theta = 89.5°$, which, for the parameters we have, show a transition from a turbulent nonlinear solution to a nonlinear solution dominated by a fundamental mode. The agreement between the two codes is very good, especially when θ gets closer to 90° (at $\theta = 89.5°$), where the fluid approximation used for the ions by Manfredi et al. (1998) is more valid. The suppression of turbulence is essentially the effect of energy flowing to the longest wavelength available in the system, when θ gets closer to 90° This is reflected by the potential evolving to a profile in the y direction that is close to a half-sine shape, as in Fig. 13, and the fundamental mode dominating in the periodic x direction. We note at this point that, from (12) and (13), we have for the electrons

$$\alpha = \frac{\Delta v_\parallel^2}{\Delta y^2} = \frac{\omega_{ce}^2}{\tan^2\theta}.$$

For $\theta = 89°$, for our set of parameters, we have $\alpha = 0.45$, while for $\theta = 89.5°$ we have $\alpha = 0.11$. The diffusion in space is much more important than the diffusion in velocity space at $\theta = 89.5°$. We observe in this case the beginning of an inverse cascade, where the fundamental k mode in the periodic direction dominates, and the potential in the y direction is evolving to a profile close to a half-sine. Hence the value of α seems to separate the regime where diffusion in velocity space is dominant or important (kinetic regime, $\alpha > 1$) from the regime where diffusion in real space is important (fluid regime, $\alpha \ll 1$), and it could be determinant in the appearance of an inverse cascade.

In Sec. 5, we have studied the effect of a small spatial-diffusion term on the solution, which is relevant to both the numerical and physical aspects of the problem. We have shown that this small diffusion term has an important effect on the physics of redistributing the charge separation on the edge of the plasma, and can significantly enhance the radial electric field and the rotation associated with the edge.

Acknowledgements

The Centre Canadien de Fusion Magnétique is funded by Hydro-Québec and the Institut national de la recherche scientifique.

Appendix. The numerical code

Time is normalized to ω_{pe}^{-1}, space to λ_{De} and velocity to v_{te}. With this normalization, the electron Vlasov equation reads as follows:

$$\frac{\partial f_e}{\partial t} + v_\parallel \cos\theta \frac{f_e}{\partial x} + E_y \frac{\sin\theta}{\Omega}\frac{\partial f_e}{\partial x} - \frac{E_x \sin\theta}{\Omega}\frac{\partial f_e}{\partial y} - E_x cos\,\theta \frac{\partial f_e}{\partial v_\parallel} = \nu_e \nabla^2 f_e, \qquad \text{(A 1)}$$

https://doi.org/10.1017/S0022377898007338 Published online by Cambridge University Press

where $\Omega = \omega_{ce}/\omega_{pe}$. We have neglected the electron polarization drift and the electron gyroradius. The ion Vlasov equation is as follows:

$$\frac{\partial f_i}{\partial t}+\Bigg\{v_\parallel\cos\theta+E_y^*\frac{\sin\theta}{\Omega}$$
$$+\frac{M\sin^2\theta}{\Omega^2}\left[\frac{\partial E_x^*}{\partial t}+v_\parallel\cos\theta\frac{\partial E_x^*}{\partial x}+\frac{\sin\theta}{\Omega}\left(E_y^*\frac{\partial E_x^*}{\partial x}-E_x^*\frac{\partial E_x^*}{\partial y}\right)\right]\Bigg\}\frac{\partial f_i}{\partial x}$$
$$+\left\{-\frac{E_x^*\sin\theta}{\Omega}+\frac{M}{\Omega^2}\left[\frac{\partial E_y^*}{\partial t}+v_\parallel\cos\theta\frac{\partial E_y^*}{\partial x}+\frac{\sin\theta}{\Omega}\left(E_y^*\frac{\partial E_y^*}{\partial x}-E_x^*\frac{\partial E_y^*}{\partial y}\right)\right]\right\}\frac{\partial f_i}{\partial y}$$
$$+E_x^*\cos\theta\frac{\partial f_i}{\partial v_\parallel}$$
$$=\nu_i\nabla^2 f_i-\frac{Mf_i}{\Omega^2}\Bigg\{\frac{\partial}{\partial t}\left(\sin^2\theta\frac{\partial E_x^*}{\partial x}+\frac{\partial E_y^*}{\partial y}\right)+v_\parallel\cos\theta\frac{\partial^2 E_x^*}{\partial y^2}$$
$$+\sin^2\theta\left[v_\parallel\cos\theta\frac{\partial^2 E_x^*}{\partial x^2}+\frac{\sin\theta}{\Omega}\left(E_y^*\frac{\partial^2 E_x^*}{\partial x^2}-E_x^*\frac{\partial^2 E_y^*}{\partial x^2}\right)\right]$$
$$+\frac{\sin\theta}{\Omega}\left(E_y^*\frac{\partial^2 E_x^*}{\partial y^2}-E_x^*\frac{\partial^2 E_y^*}{\partial y^2}\right)\Bigg\}. \tag{A 2}$$

The asterisk indicates the smoothing operation presented in (2), and $M = m_i/m_e$. The numerical technique is based on a splitting algorithm (which separates the evolution in the x, y and $v_\parallel$ directions). The distribution function is advanced as follows (we present the details for (A 2): (A 1) is treated in a similar way.

1. Solve for $\Delta t/2$

$$\frac{\partial f_i}{\partial t}+E_x^*\cos\theta\frac{\partial f}{\partial v_\parallel}=0. \tag{A 3}$$

The solution of (A 3) is

$$f_i(t+\Delta t/2)=f_i(x,y,v_\parallel-E_x\cos\theta\,\Delta t/2).$$

2. Solve for $\Delta t/2$

$$\frac{\partial f_i}{\partial t}+\Bigg\{v_\parallel\cos\theta+E_y^*\frac{\sin\theta}{\Omega}+\frac{M\sin^2\theta}{\Omega^2}\left[\frac{\partial E_x^*}{\partial t}+v_\parallel\cos\theta\frac{\partial E_x^*}{\partial x}\right.$$
$$\left.+\frac{\sin\theta}{\Omega}\left(E_y^*\frac{\partial E_x^*}{\partial x}-E_x^*\frac{\partial E_x^*}{\partial y}\right)\right]\Bigg\}\frac{\partial f_i}{\partial x}=0. \tag{A 4}$$

The solution of (A 4) is

$$f_i^+=f_i(x-\delta x,y,v_\parallel,t),$$

where δx is the term in braces in (A 4), multiplied by $\Delta t/2$.

https://doi.org/10.1017/S0022377898007338 Published online by Cambridge University Press

3. Solve for $\Delta t/2$

$$\frac{\partial f_i^{++}}{\partial t}+\left\{-\frac{E_x^*\sin\theta}{\Omega}+\frac{M}{\Omega^2}\left[\frac{\partial E_y^*}{\partial t}+v_\parallel\cos\theta\frac{\partial E_y^*}{\partial x}\right.\right.$$
$$\left.\left.+\frac{\sin\theta}{\Omega}\left(E_y^*\frac{\partial E_y^*}{\partial x}-E_x^*\frac{\partial E_y^*}{\partial y}\right)\right]\right\}\frac{\partial f_i}{\partial y}=0. \quad \text{(A 5)}$$

The solution of (A 5) is

$$f_i=f_i(x,y-\delta y,v_\parallel),$$

where δy is the term in braces in (A 5), multiplied by $\Delta t/2$.

4. Solve for $\Delta t/2$

$$\frac{\partial f_i}{\partial t}=\nu_i\nabla^2 f_i-\frac{M}{\Omega^2}\left\{\frac{\partial}{\partial t}\left(\sin^2\theta\frac{\partial E_x^*}{\partial x}+\frac{\partial E_y^*}{\partial y}\right)+v_\parallel\cos\theta\frac{\partial^2 E_x^*}{\partial y^2}\right.$$
$$+\sin^2\theta\left[v_\parallel\cos\theta\frac{\partial^2 E_x^*}{\partial x^2}+\frac{\sin\theta}{\Omega}\left(E_y^*\frac{\partial^2 E_x^*}{\partial x^2}-E_x^*\frac{\partial^2 E_y^*}{\partial x^2}\right)\right]$$
$$\left.+\frac{\sin\theta}{\Omega}\left(E_y^*\frac{\partial^2 E_x^*}{\partial y^2}-E_x^*\frac{\partial^2 E_y^*}{\partial y^2}\right)\right\}f_i. \quad \text{(A 6)}$$

Equation (A 6) is solved for $\Delta t/2$ as follows:

$$f_i\left(t+\frac{\Delta t}{2}\right)=f_i^{++}\exp\left\{-\frac{M}{\Omega^2}\left[\sin^2\theta\left(\frac{\partial E_x^{*+}}{\partial x}-\frac{\partial E_x^{*-}}{\partial x}\right)\right.\right.$$
$$\left.\left.+\frac{\partial E_y^{*+}}{\partial y}-\frac{\partial E_y^{*-}}{\partial y}+\frac{\nu_i}{f_i^{++}}\nabla^2 f_i^{++}\frac{\Delta t}{2}\right\}\right.$$
$$\times\exp\left\{-\frac{\Delta t}{2}v_\parallel\cos\theta\frac{\partial^2 E_x^*}{\partial y^2}-\frac{\Delta t}{2}\sin^2\theta\left[v_\parallel\cos\theta\frac{\partial^2 E_x^*}{\partial x^2}\right.\right.$$
$$\left.+\frac{\sin\theta}{\Omega}\left(E_y^*\frac{\partial^2 E_x^*}{\partial x^2}-E_x^*\frac{\partial^2 E_y^*}{\partial x^2}\right)\right]$$
$$\left.-\frac{\Delta t}{2}\frac{\sin\theta}{\Omega}\left(E_y^*\frac{\partial^2 E_x^*}{\partial y^2}-E_x^*\frac{\partial^2 E_y^*}{\partial y^2}\right)\right\}. \quad \text{(A 7)}$$

The superscripts + and − on the electric field indicate the present value of the electric field and the value calculated right before Step 1.

5. Solve the Poisson equation at time $t+\Delta t/2$. This equation is solved using the method presented in Shoucri et al. (1997, 1998) with zero boundary conditions for ϕ. The equation, in dimensionless units, is given by

$$\nabla^2\phi=-n_i^*+n_e. \quad \text{(A 8)}$$

The electric field is calculated from ϕ through the relation $\mathbf{E}=-\boldsymbol{\nabla}\phi$. This is subsequently smoothed using the filtering operator in (2) to give $\mathbf{E}^*$ when advancing the ions in time.

6. Repeat Step 4.

7. Repeat Step 3.

https://doi.org/10.1017/S0022377898007338 Published online by Cambridge University Press

8. Repeat step 2.
9. Repeat step 1.
10. Repeat Step 5 to solve for the electric field.

One then goes back to Step 1 and repeats the cycle. Each cycle advances the distribution function by one time-step. Note that the Poisson equation is solved twice per cycle: at t and $t+\Delta t/2$.

References

Burrell, K. H., Carlstrom, T. N., Doyle, E. J., Gohil, P., Groalner, R. H. et al. 1990 *Phys. Fluids* **32**, 1405.

Ghizzo, A., Bertrand, P., Shoucri, M., Fijalkow, E. and Feix, M. R. 1993 *J. Comput. Phys.* **108**, 105.

Knorr, G. and Pécseli, H. 1989 *J. Plasma Phys.* **41**, 157.

Manfredi, G., Shoucri, M., Dendy, R., Ghizzo, A. and Bertrand, P. 1996 *Phys. Plasmas* **3**, 202.

Manfredi, G., Shoucri, M., Bertrand, P., Ghizzo, A., Lebas, J., Knorr, G. et al. 1998 *Physica Scripta* **58**, 159.

Shoucri, M., Lebas, J., Knorr, G., Bertrand, P., Ghizzo, A., Manfredi, G. and Christofer, I. 1997 *Physica Scripta* **55**, 617.

Shoucri, M., Lebas, J., Knorr, G., Bertrand, P., Ghizzo, A., Manfredi, G. and Christofer, I. 1998 *Physica Scripta* **57**, 283.

Weynants, R. R., Van Oost, G. et al. 1992 *Nucl. Fusion* **32**, 837.